Assessment of a Shallow Water Model using a Linear Turbulence Model for Obstruction-Induced Discontinuous Flows

Jaan Hui Pu*, Zhumabay Bakenov, Desmond Adair

School of Engineering, Nazarbayev University
53, Kabanbay batyr Ave., Astana, 010000, Republic of Kazakhstan

Abstract

Assessment of the performance of a shallow water model with closure using a linear *k-ε* turbulence model is made for various obstruction-induced discontinuous flows. The monotone upwind scheme of conservative laws (MUSCL) - Hancock scheme is used, together with the Harten Lax van Leer (HLL) approximate Riemann solver in the discretization of the finite volume shallow water model. These kinds of models contribute to the improvement of optimized design of various processes in chemical engineering and technology. Two obstructed flow applications are presented, namely, single obstruction and multiple obstruction induced discontinuous flows; and the ability of the shallow water model with the *k-ε* based turbulence model to predict these applications are assessed. The simulation results of the shallow water model are compared with those found by direct numerical simulation (DNS) and experimental measurements in the literature.

Introduction

In recent years, a variety of numerical schemes and models have been used to simulate the water flow in channels and estuaries. Numerical models to compute the free surface flows by solving depth-averaged, two-dimensional unsteady flow equations have been considered by many authors (e.g. Tseng, 1999, Horritt, 2004, and Lai et al., 2005), with good results ensuing. Different turbulence models to simulate turbulence properties have also been developed for a variety of flow applications. The standard *k-ε* model, first described by Launder and Spalding (1974), and, Rodi (1980), has enjoyed considerable success in representing turbulent flow characteristics, and, a number of investigations, using the *k-ε* model, have been carried out by Younus and Chaudhry (1994), and Stansby (1997), and more recently by Jiang et al. (2009), and Sana et al. (2009).

However, it is now known that the most important defects of the standard turbulence *k-ε* model occur in the modelling of the Reynolds stresses using the linear Boussinesq stress-strain relationship. This is an unrealistic representation of normal stress anisotropy, common to almost all shear flows, and the results in substantial errors in complex strain, as the gradients of the normal stresses contributed significantly to the momentum balance. Other predictive deficiencies for the standard *k-ε* model include poor sensitivity to curvature strain and dilation, excessive levels of turbulence in regions of strong normal straining, the wrong response to swirl and the suppression of self-induced periodic motions.

Various researchers have contributed to the investigation of obstruction-induced flow using *k-ε* turbulence models. Bosch and Rodi (1998) calculated single-obstruction flow using the standard *k-ε* model, by looking at flow over a cylinder. Lee (1998) developed a numerical prediction method for the early transient stage of single-obstruction flow. In more recent research, Jiang et al. (2009) have investigated the turbulent shallow wake region with emphasis on the near wake of the obstruction. However, no assessment studies have been done in those studies to the utilisation of the energy and dissipation transport equations to simulation flow turbulence.

*corresponding author. Email: jhpu@nu.edu.kz

 Printed in Kazakhstan

Since the inclusion of turbulent models is crucial in many flow applications, where the non-steady and sudden flow viscosity variation is dominant, a linear *k-ε* model is used and appraised together with the depth averaged shallow water model in this paper in an attempt to fully capture and re-produce the obstructed water flow behaviour. Besides, the conventional single-block obstruction induced discontinuous flow, the proposed model is also tested against the multi-obstruction flows. The modelling competence of the *k-ε* model is then determined by comparing the simulation results with DNS (direct numerical simulations) and experimental measurements. The analysis is aimed at establishing a guideline as to the ability and limits of the *k-ε* model.

Governing Equations

Shallow Water Model

The full two-dimensional depth averaged shallow water equations used in this study can be expressed as

$$\frac{\partial \varphi}{\partial t} + \frac{\partial (\varphi u_i)}{\partial x_i} = 0 \tag{1}$$

$$\frac{\partial (\varphi u_i)}{\partial t} + \frac{\partial \left(\varphi u_j u_i\right)}{\partial x_j} = \frac{\partial}{\partial x_j}\left[\varphi T_{ij}\right] + g\varphi\left(S_{0x} - S_{fx}\right) \tag{2}$$

$$T_{ij} = \vartheta_t \left[\frac{\partial (\varphi u_i)}{\partial x_j} + \frac{\partial \left(\varphi u_j\right)}{\partial x_i}\right] - \frac{2}{3} k \delta_{ij} \tag{3}$$

The variable φ is the geopotential, and it is given by $\varphi = g \cdot h$; h is the water depth; g is the acceleration due to gravity; ϑ_t is the eddy viscosity due to turbulence, k is the energy and δ_{ij} is the Kronecker delta. The bed slope and bed shear stress of the channel are given by S_0 and S_f

$$S_{0x_i} = -\frac{\partial z_g}{\partial x_i}, \quad S_{0x_j} = -\frac{\partial z_g}{\partial x_j}, \quad S_{fx_i} = \frac{n^2 u_i \sqrt{u_i^2 + u_j^2}}{h^{4/3}}, \quad S_{fx_j} = \frac{n^2 u_j \sqrt{u_i^2 + u_j^2}}{h^{4/3}}, \tag{4}$$

where, z_g is the bed surface geometrical elevation; and n is the Manning friction coefficient;

Standard k-ε Turbulence Model

The depth-averaged eddy viscosity due to turbulence is calculated in the standard *k-ε* with

$$\vartheta_t = C_\mu \frac{k^2}{\varepsilon} \tag{5}$$

where C_μ is an empirical constant. The turbulence energy k and its dissipation rate ε are determined using

$$\frac{\partial k}{\partial t} + \frac{\partial \left(u_j k\right)}{\partial x_j} = \frac{\partial}{\partial x_j}\left[\frac{\vartheta_t}{\sigma_k}\frac{\partial k}{\partial x_j}\right] + g \cdot R_h + g \cdot R_k - \varepsilon \tag{6}$$

$$\frac{\partial \varepsilon}{\partial t} + \frac{\partial \left(u_j \varepsilon\right)}{\partial x_j} = \frac{\partial}{\partial x_j}\left[\frac{\vartheta_t}{\sigma_\varepsilon}\frac{\partial \varepsilon}{\partial x_j}\right] + \frac{\varepsilon}{k}\left(g \cdot C_{1\varepsilon} \cdot R_h - C_{2\varepsilon} \cdot \varepsilon\right) + g \cdot R_\varepsilon \tag{7}$$

The parameters $R_{h,}$ R_k and R_ε are as follows

$$R_h = \frac{\vartheta_t}{h}\left\{2\left[\frac{\partial u_i}{\partial x_i}\right]^2 + 2\left[\frac{\partial u_j}{\partial x_j}\right]^2 + \left[\frac{\partial u_i}{\partial x_j} + \frac{\partial u_j}{\partial x_i}\right]^2\right\} \tag{8}$$

$$R_k = \frac{g}{C^2}\left(u_i^2 + u_j^2\right)^{\frac{3}{2}} \tag{9}$$

$$R_\varepsilon = \frac{C_{2\varepsilon} C_\mu g^{\frac{5}{4}}\left(u_i^2 + u_j^2\right)^2}{h D^{\frac{1}{2}} C^{\frac{5}{2}}} \tag{10}$$

Standard values are used for the parameters shown in the equations above, and are given as follows

$C =$ Chezy Coefficient $= h^{1/6}/n$, $C_\mu = 09$, $C_{1\varepsilon} = 1.44, C_{2\varepsilon} = 1.92, \sigma_k = 1.0, \sigma_\varepsilon = 1.3$, $D = 1.0$.

Numerical Scheme

In this study, the FV method was used to model the proposed the obstruction-induced flow as it is robust in simulating high dimensional shock wave accurately (Mingham and Causon, 2000, and Sanders, 2001). The inviscid flux was modelled

using a Godunov-type Hancock scheme with a two-stage predictor-corrector temporal discretization. The Godunov-type Hancock scheme was coupled with Harten Lax van Leer (HLL) approximate Riemann solver for updating volumetric discretization. The slope limiter method was used in the HLL solver to ensure the space discretization scheme satisfies flux-limiting property to eliminate the spurious oscillations.

Approximate Riemann Solver

Exact Riemann solvers are computationally expensive, particularly for non-linear systems. Fortunately, a number of computationally inexpensive approximate Riemann solvers have been developed, such as Roe's Solver – Roe (1981), Osher's Solver – Osher and Solomone (1982), and HLL Solver – Harten et al (1983). In this paper, the HLL approximate solver has been used due to its accuracy to resolve the interface computational wave speeds.

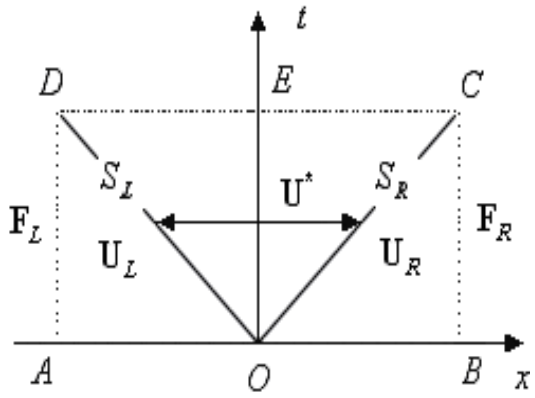

Fig. 1. HLL approximate Riemann solution cell.

Consider the HLL solution cell shown at Figure 1, $S_L \le 0$ and $S_R \ge 0$ are a-priori estimates for the lower and upper bounds of the wave speed. Subscripts L and R represent left and right-region of the solution cell respectively; and superscript * represents star region of the solution cell. The inviscid solution of the indicated cell can be written in conservation form as

$$\oint_c [\mathbf{F}dt - \mathbf{U}dx] = 0 \tag{11}$$

where, $\mathbf{F}$ represents the numerical flux vector of the solution cell. From equation (11), one can obtain the following expression for the star region $\mathbf{U}$ variables (Toro, 1999)

$$\mathbf{U}^* = \begin{cases} \mathbf{U_L}, & S_L > 0 \\ \mathbf{U_{HLL}}, & S_L \le 0 < S_R \\ \mathbf{U_R}, & S_R \le 0 \end{cases} \tag{12}$$

where,

$$\mathbf{U}_{HLL} = \frac{S_R\mathbf{U_R} - S_L\mathbf{U_L} - (\mathbf{F_R} - \mathbf{F_L})}{S_R - S_L} \tag{13}$$

The expression for the numerical flux could then be given by

$$\mathbf{F}^* = \begin{cases} \mathbf{F_L}, & S_L \ge 0 \\ \mathbf{F_{HLL}}, & S_L \le 0 \le S_R \\ \mathbf{F_R}, & S_R \le 0 \end{cases} \tag{14}$$

where,

$$\mathbf{F}_{HLL} = \frac{S_R\mathbf{F_L} - S_L\mathbf{F_R} + S_LS_R(\mathbf{U_R} - \mathbf{U_L})}{S_R - S_L} \tag{15}$$

Wave speeds, S_L and S_R in equations (13) and (15) can be expressed as

$$S_L = \min\left[u_L - c_L,\ u^* - c^*\right] \tag{16}$$

$$S_R = \min\left[u_R + c_R,\ u^* + c^*\right] \tag{17}$$

where, u^*, and c^* in the star region are estimated as (c is the celerity wave, in which $c = \sqrt{\varphi}$)

$$u^* = \frac{(u_L + u_R)}{2} + c_L - c_R \tag{18}$$

$$c^* = \frac{(c_L + c_R)}{2} + \frac{(u_L - u_R)}{4} \tag{19}$$

For a dry bed scenario, extra conditions are needed for S_L and S_R, and these conditions are

For the left dry bed ($h_L = 0$)

$$S_L = u_R - 2c_R \tag{20}$$

$$S_R = u_R + c_R \tag{21}$$

For the right dry bed ($h_R = 0$)

$$S_L = u_L - c_L \tag{22}$$

$$S_R = u_L + 2c_L \tag{23}$$

Monotone Upwind Scheme for Conservation Laws (MUSCL) and Hancock Scheme

In the most primitive Godunov scheme, a constant approximation was used for the increments of $\mathbf{U}_L$ and $\mathbf{U}_R$ in time. This assumption has shown to deflect the flow numerical flux away from the actual wave solution throughout time increment. In this study, a more robust numerical wave updating scheme, MUSCL scheme, was used, which both $\mathbf{U}_L$ and $\mathbf{U}_R$ are changing linearly according to their adjacent cells. The MUSCL scheme gives a second order of accuracy to the proposed FV model, and it is expressed as

$$\mathbf{U}_L = \mathbf{U}_i - \frac{1}{2}\cdot\Psi\left(\tilde{r}_i\right)\cdot\Delta\hat{\mathbf{U}}_{i-1/2}, \text{ and,}$$
$$\mathbf{U}_R = \mathbf{U}_i + \frac{1}{2}\cdot\Psi\left(\tilde{r}_{i+1/2}\right)\cdot\Delta\hat{\mathbf{U}}_{i+1/2} \tag{24}$$

where,

$$\tilde{r}_i = \frac{\Delta\hat{\mathbf{U}}_{i+1/2}}{\Delta\hat{\mathbf{U}}_{i-1/2}},\ \Delta\hat{\mathbf{U}}_{i+1/2} = \mathbf{U}_{i+1} - \mathbf{U}_i, \text{ and,}$$
$$\Delta\hat{\mathbf{U}}_{i-1/2} = \mathbf{U}_i - \mathbf{U}_{i-1} \tag{25}$$

In equations (24) – (25), Ψ is the slope limiter; and, i represents the space step. The van Leer limiter was adopted in this paper as it was identified to be the best slope limiter to minimize the numerical over- or undershoot (Toro, 1999, and Pu, 2008), where $\Psi = \left[r + |r|\right]/\left(1 + r\right)$. A Hancock two-stage predictor-corrector scheme was utilised to update $\mathbf{U}_i$. It has the ability to maintain stability and to achieve second order of accuracy in the temporal domain. The two steps are given as

Predictor Step

$$\mathbf{U}_i^{N+1/2} = \mathbf{U}_i^N - \frac{\Delta t}{2\Omega_i}\left(\mathbf{F}_i^N - \mathbf{F}_{i-1}^N\right) \tag{26}$$

Corrector Step

$$\mathbf{U}_i^{N+1} = \mathbf{U}_i^N - \frac{\Delta t}{\Omega_i}\left(\mathbf{F}_{i+1}^{N+1/2} - \mathbf{F}_i^{N+1/2}\right) \tag{27}$$

$$\mathbf{U}_i^{N+1} = \mathbf{U}_i^N - \Delta t\left(\mathbf{Q}_i^N\right) \tag{28}$$

Ω is the cell volume; and N represents the time step. A stability criterion, Courant-Friedrichs-Lewy criterion, was chosen to ensure Δt does not exceed its maximum allowable limit, and it is given as

$$\Delta t \le C_{FL}\left[\frac{\Omega}{|\boldsymbol{q}\cdot\boldsymbol{s}| + c\cdot|\boldsymbol{s}|}\right] \tag{29}$$

where, $\boldsymbol{q}\cdot\boldsymbol{s} = u\cdot\boldsymbol{s}_x + v\cdot\boldsymbol{s}_y$; $\boldsymbol{s}$ represents resultant normal unit vector; $\boldsymbol{s}_x$ and $\boldsymbol{s}_y$ represent normal unit vectors in streamwise and transverse directions respectively; and, C_{FL} is the Courant number, which is limited to $0 < C_{FL} \le 1$. Smaller C_{FL} can give more accurate and stable results, but at an increasing computational cost.

Boundary Conditions

In this paper, two ghost cells were used outside the computational space domain to implement the boundary conditions. Two types of boundary were used, open and solid boundaries. The boundary vectors, $\mathbf{U}^B$, can be written as

Open Boundaries

$$\boldsymbol{U}^B = \left[\phi \quad \phi u \quad \phi v \quad \phi u_s^2/\sqrt{c_\mu} \quad \phi u_s^3/\left[\kappa\left(z - z_o\right)\right]\right]^T \tag{30}$$

Solid Boundaries

$$\boldsymbol{U}^B = \left[\phi \quad -\phi u \quad -\phi v \quad \phi u_s^2/\sqrt{c_\mu} \quad \phi u_s^3/\left[\kappa\left(z - z_o\right)\right]\right]^T \tag{31}$$

These boundaries were updated by using

$$\mathbf{U}^{\boldsymbol{B}}_{m+1} = \mathbf{U}^{\boldsymbol{B}}_{m}, \text{ and, } \mathbf{U}^{\boldsymbol{B}}_{m+2} = \mathbf{U}^{\boldsymbol{B}}_{m-1} \tag{32}$$

In equations (30) – (32), m is the boundary node; the friction velocity of the flow, $u_s = n/h^{1/6}\sqrt{g\left(u^2+v^2\right)}$; the turbulent flow region from the bed, $z - z_o = z_p v u_s$; where z_p is the wall region characteristic length, which is dependant on the wall condition. In this paper, a value of $11.6 \le z_p \le 100$ was used (see Pu, 2008).

Initial Conditions

The initial conditions for water height, and velocities are varied and dependant on the different investigated applications. However, for the energy and energy dissipation, the initial conditions used are given as

$$\varepsilon_I = S_o g u_I \tag{33}$$

$$k_I = \left(0.0765 \frac{\varepsilon_I}{C_\mu} \frac{\phi_I u_I}{C} \right) \tag{34}$$

where, subscript I represents the initial condition.

Results and Discussions

The proposed *k-ε* model was applied to turbulent flow applications with the existence of obstructions. Two tests were discussed in this section. A single rectangular-block obstacle was used in the first application; and three rectangular-block obstacles (multiple obstructions) were used in the second application to create the discontinuous flows. Both tests were also compared against existing results from the literatures (e.g. Wissink, 1997, and Kabir et al., 2004).

Single-Obstruction Flow

In this test, a channel (12 m wide and 14 m long) with a 1 × 1 m rectangular-block obstacle positioned along the flow was investigated as shown on Figure 2. Initially, the water depth, streamwise velocity and lateral velocity were set at 1.0 m, 1.0 m/s and 1.0×10^{-6} m/s respectively. Also, it is assumed that there were no energy and energy dissipation initially at the start of the flow due to the uniform initial water depth and velocities assumptions. The simulation was run for 77.0 s, and the turbulent flow results are presented on Figures 3 and 4. Figure 3 shows a contour plot of water height with flow vector. One can observe that the water is at its highest level (super-elevation) at the front of the block, and at its lowest level at the rear. The same effect could also be referred to on Figure 4 of the flow wave formed. To explain this phenomenon, first the superposition of the water is achieved as the block stops the arriving water from the inlet, which creates the super-elevation at the front of the block. Then, the water declines around the block gradually until it reaches the minimum position. Since the rear of the block is hidden, no flow can directly enter there. Hence, a low-depressed water depth is observed behind the block. For full explanation of this test the reader should refer to Pu et al. (2007).

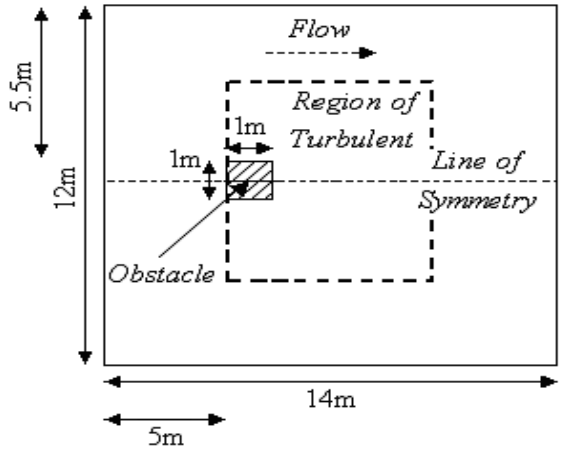

Fig. 2. Layout of single obstruction flow.

The predicted results of the single-obstruction flow were compared with the Direct Numerical Simulation (DNS) results by Wissink (1997) as shown on Figure 5. The pure shallow water simulation was also plotted to determine its difference with the *k-ε* shallow water model in simulating the obstruction-induced discontinuous flow. The u-velocity profiles comparison was taken on different positions of the region behind the block – region of turbulence (at x = 8.0 m, 9.0 m, 10.0 m, 11.0 m, and 12.0 m). The comparison demonstrates clearly that the *k-ε* function improves the shallow water model in capturing the discontinuous characteristics of the flow application.

To compare the numerical predictions of both shallow water models with the DNS results, it is interesting to present the mid-wave velocity in the progression of streamwise direction (mid-wave velocity magnitude v_{mv} according to x). On Figure 6, one could observe that the pure shallow water predictions has clearly given less consistent results compared to the DNS data; and this inconsistency has been improved by the utilisation of the *k-ε* function, which successfully implements the progressive flow viscosity variation and energy loss into the flow system.

By using equation (35) showing below, one could evaluate the numerical performance of both models against the DNS results quantitatively.

Table 1 summaries the relative error in L_2 norm, which could be defined as follows

$$L_2 = \sqrt{\frac{\sum_i \left(\mathbf{U}_i^{sim} - \mathbf{U}_i^{exact}\right)^2}{\sum_i \left(\mathbf{U}_i^{exact}\right)^2}} \tag{35}$$

where, $\mathbf{U}_i^{sim}$ and $\mathbf{U}_i^{exact}$ are the simulated numerical solution and the exact/measured data respectively. Table 1 shows that the *k-ε* function improves the DNS comparative error of the shallow water numerical solution by about 10 times when their velocities at the centred streamwise position were compared. The centre streamwise position was chosen for this comparison as it consists maximum wave variables change, which highlights the importance for the use of the proposed turbulence model.

Table 1

L_2 norm (relative error) for different flow cases

Flow Case		*R*	
		Shallow Water Model	*k-ε* Shallow Water Model
Single Obstruction		0.0597	0.0062
		$2.0 \le g/w \le 4.0$	$4.0 < g/w \le 8.0$
Multiple Obstruction	$l/b = 1.5$	0.1559	0.0211
	$l/b = 1.0$	0.2181	0.0156
	$l/b = 0.5$	0.4502	0.0281
	$l/b = 0.3$	0.5860	0.0132

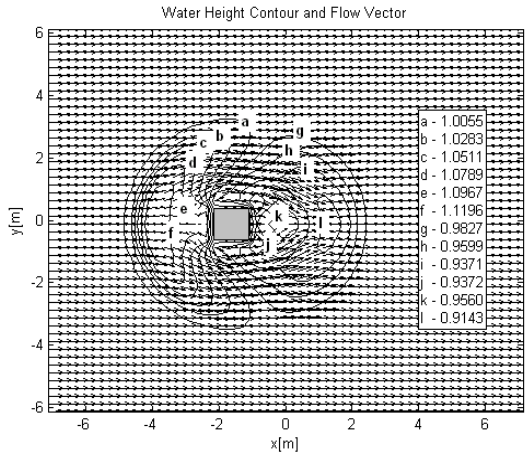

Fig. 3. Water depth contour and flow vector for single obstructed-flow (measurements in m).

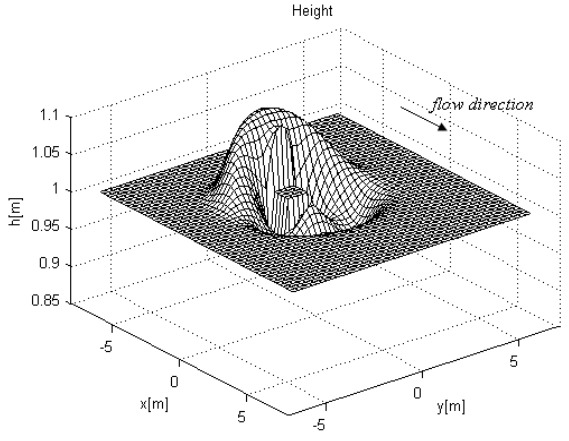

Fig. 4. Pattern of water surface elevations around the rectangular block.

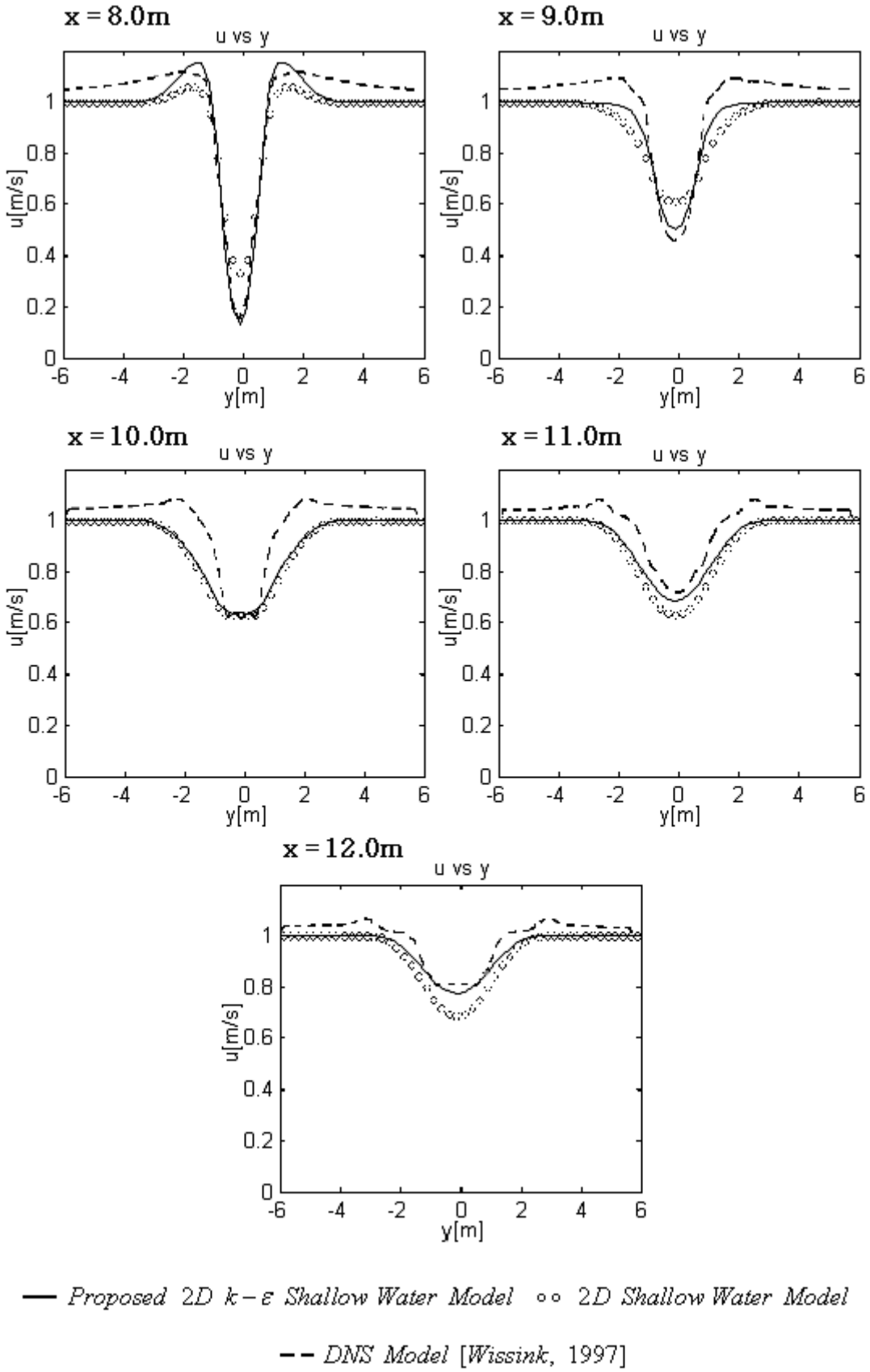

Fig. 5. Comparison of u -velocity profiles across width (y) at various streamwise positions (x = 8.0-12.0 m).

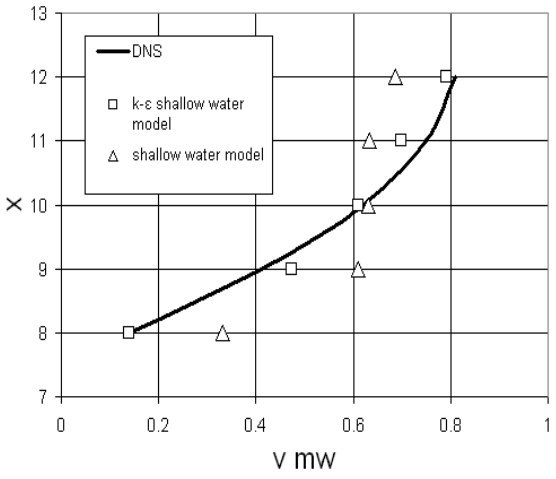

Fig. 6. Mid-wave streamwise velocities comparison.

Multi-Obstruction Flow

By having a combination of different discontinuous effects (constructive and diffusive), multiple obstructed-flow has always been a difficult phenomenon to investigate. In this paper, the proposed *k-ε* model has been used to perform multiple tests on multiple obstruction induced flows by using different obstruction dimension and size, which tested experimentally by Kabir et al. (2004).

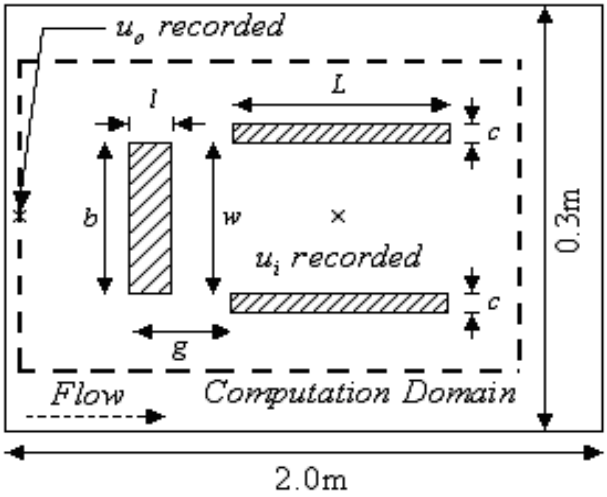

Fig. 7. Layout of multiple obstruction induced discontinuous flow.

In Kabir et al. (2004) test, the full channel has a dimension of 3m length and 0.9m width. However, the channel is bounded by guide-walls to constraint a region for flow testing of 2m length and 0.3m width, where the basic schematic diagram of this bounded region is presented on Figure 7. Three obstacles with different sizes were stationed in the channel – one $l \times b$ vertical block and two parallel $L \times c$ horizontal blocks. By referring to Figure 7, some dimensions of the channel and obstacles were fixed: $w = b = 25$ mm, $L = 200$ mm, and $c = 2.5$ mm. However, g and l were varying in the tests, where the ratios of g/w (ranging from 2.0 to 8.0) were tested for different l/b ratios (0.3, 0.5, 1.0, and 1.5). The initial conditions of water depth, streamwise velocity, transverse velocity, energy and energy dissipation used were set as $h_I = 0$ .125 m, $u_I = 0.24$ m/s, $v_I = 0$, $k_I = 0$, and $\varepsilon_I = 0$ respectively. The simulations were run until steady state condition reached.

Figure 8 a-d presents the numerical modelled flow field vector study for the effect of changing $l \times b$ vertical block size on the multiple obstructed-flow. The tests were run for the different l/b ratios of 0.3, 0.5, 1.0, and 1.5. As a comparatively result, the most chaotic flow field condition happens at $l/b = 0.3$; while the most stable flow occurs at $l/b = 1.5$. In other words, the increase of the vertical block size could stabilize the flow. The enlarged diagrams of the flow field vector with obstructions dimension of $g/w = 8.0$ and $l/b = 1.5$ are presented on Figure 9 (a-b). One could observe that the turbulent eddies created at the back of the vertical block causing chaotic flow vorticity behaviour. It also shows that the flow circulation happens around the block before reaching the back of the obstruction. Figure 10 shows the investigation of the effect for changing the vertical block location.

The flow field (on Figure 10 a-g) shows that smaller gap ratio g/w creates more chaotic flow behind the vertical block, and this effect could be stabilized by the bigger gap ratio g/w. The flow field in the enlarged diagram (Figure 11 a-b) for the obstruction dimension of $g/w = 2.0$, and $l/b = 1.5$ allows clear demonstration of the above-mentioned argument, where the flow field at the back of the vertical block is appeared to be chaotic and influenced by the turbulent eddies.

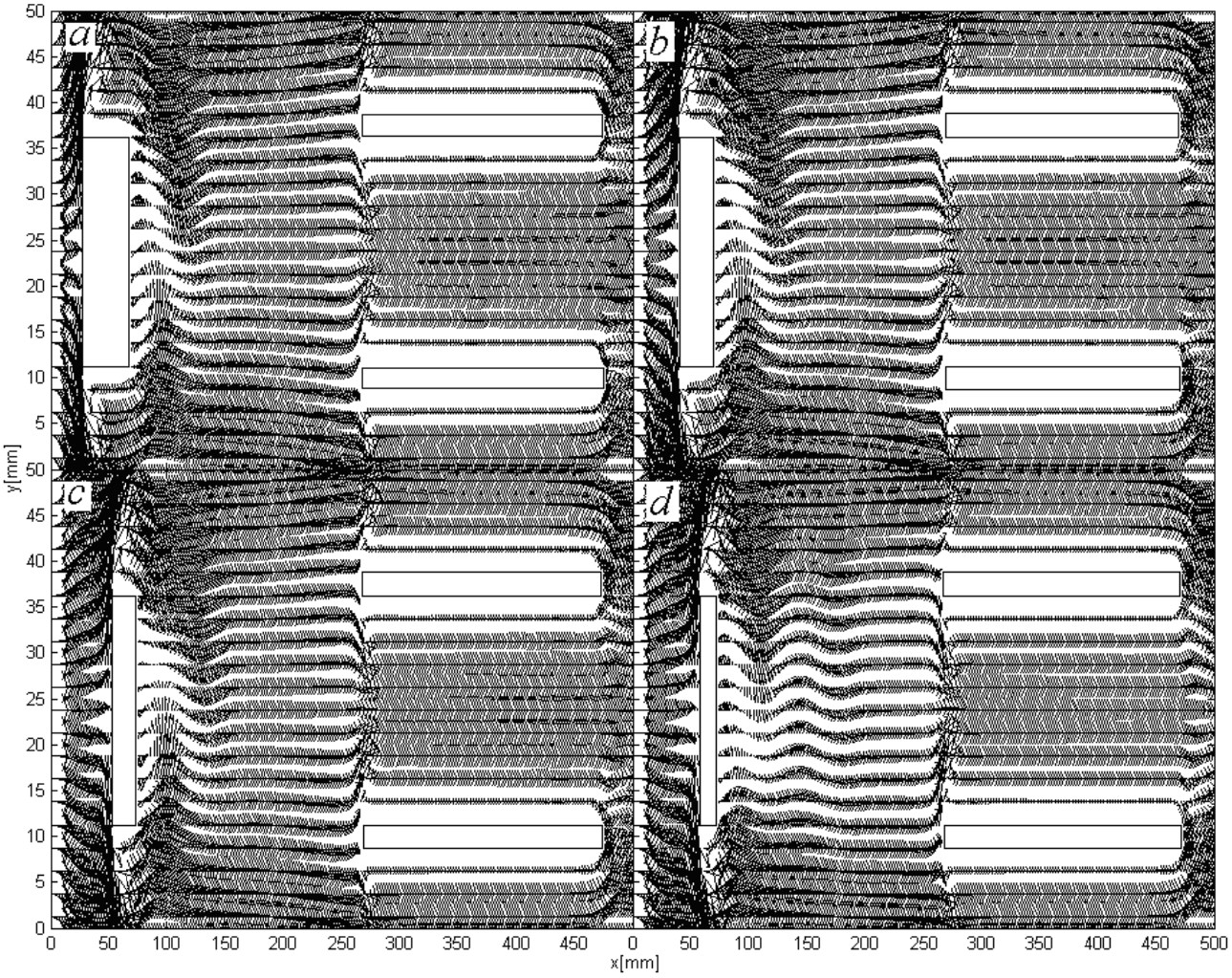

Fig. 8. Flow field vector simulated (to investigate the effect of changing the vertical block size) with: a) *g/w* = 8.0 and *l/b=1.5*; b) *g/w* = 8.0, and *l/b*=1.0; c) *g/w* = 8.0, and *l/b* = 0.5; d) *g/w* = 8.0, and *l/b* = 0.3.

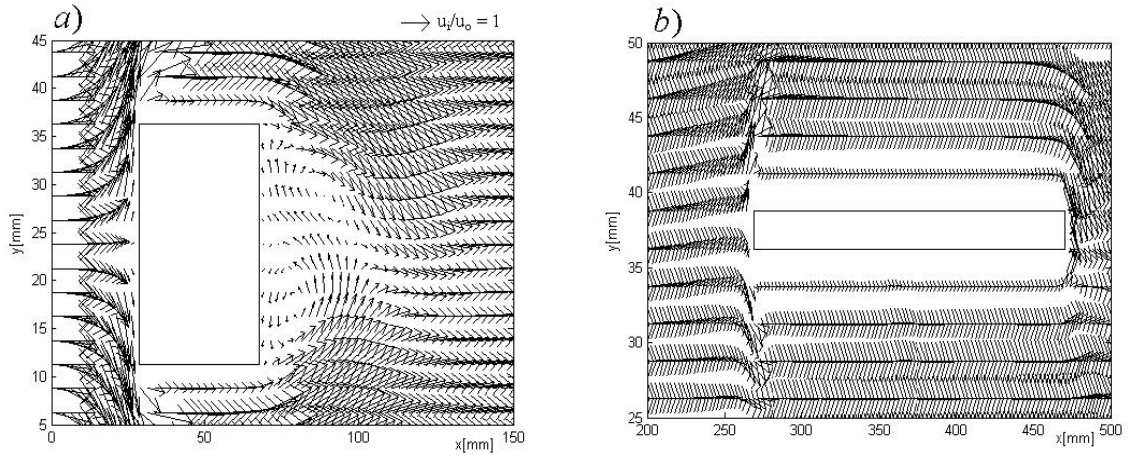

Fig. 9. Enlarged portions of the flow on Figure 10 (a) with dimensions of *g/w* = 8.0 and *l/b* = 1.5: a) flow around the vertical block, and b) flow around the parallel horizontal block.

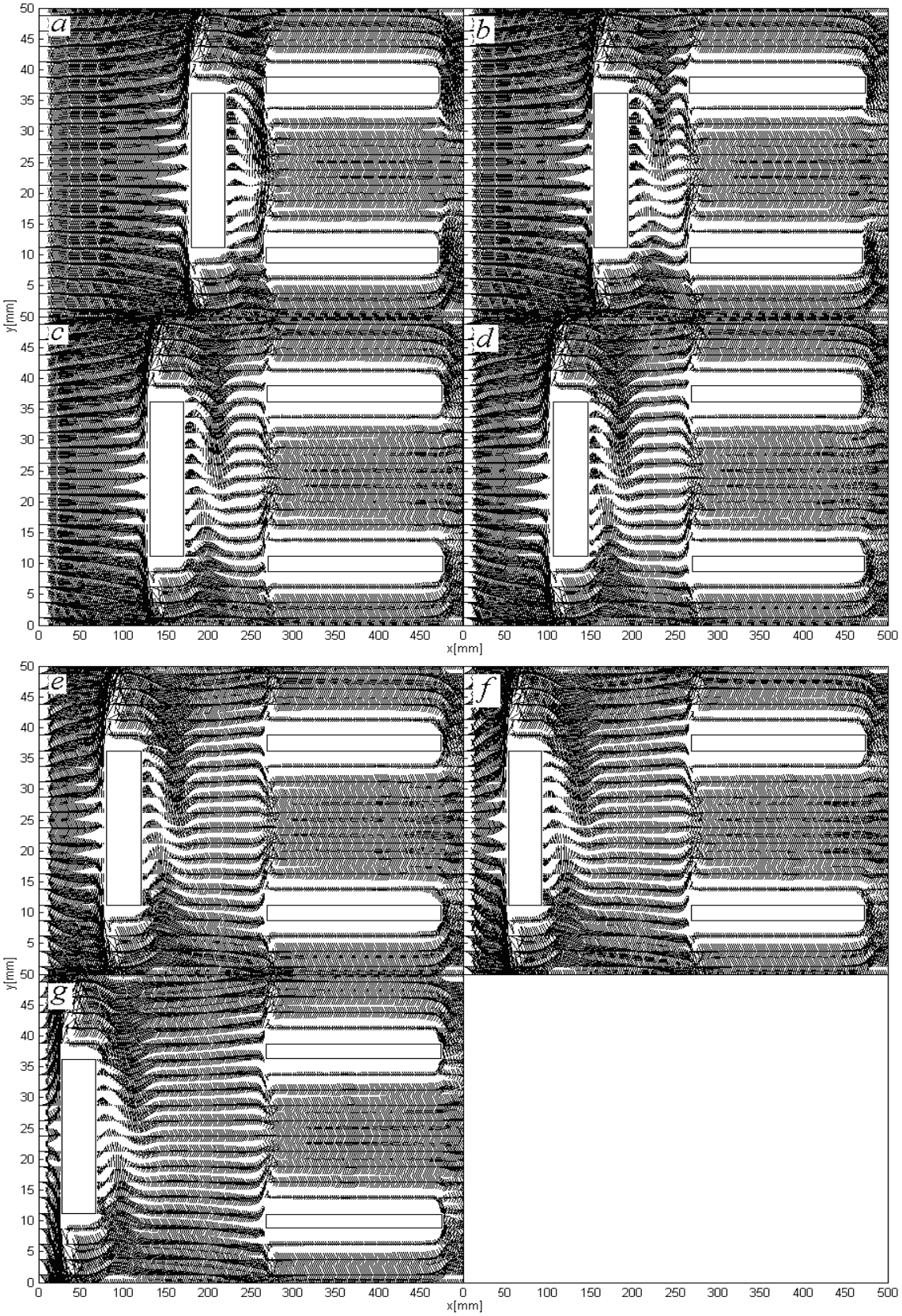

Fig. 10. Flow field vector simulated (to investigate the effect of changing the vertical block location) with: a) *g/w* = 2/0, and *l/b* = 1.5; b) *g/w*=3.0, and *l/b* = 1.5; c) *g/w* = 4.0, and *l/b* = 1.5; d) *g/w* = 5.0, and l/b = 1.5; e) *g/w* – 6.0, and *l/b* = 1.5; f) *g/w* = 7.0, and *l/b* = 1.5; g) *g/w* = 8.0, and *l/b* = 1/5.

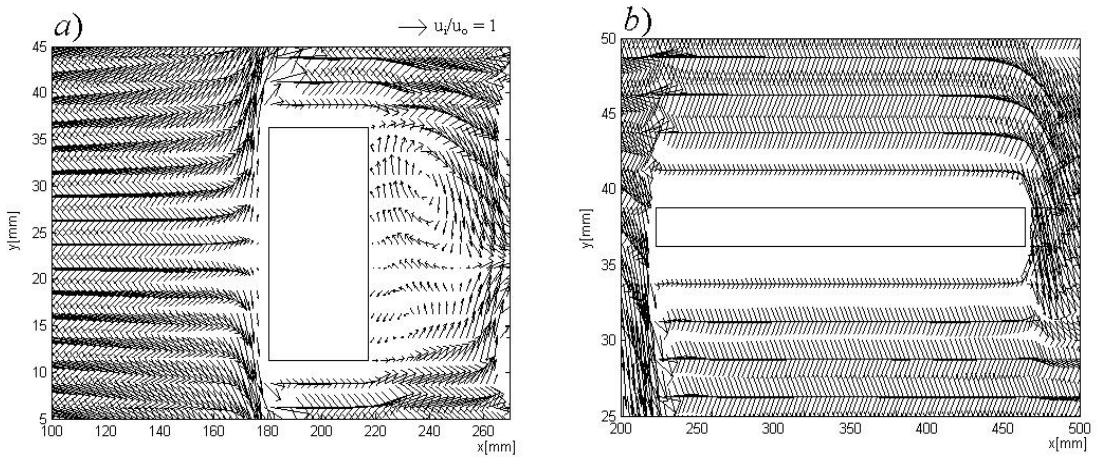

Fig. 11. Enlarged portions of the flow on Figure 12 (a) with dimensions of g/w = 2.0, and l/b = 1.5: a) flow around the vertical block, and b) flow around the parallel horizontal block.

Figure 12 shows the predicted simulation results of u_i/u_o compare with the experimental measurements by Kabir et al. (2004). The u_o is the velocity recorded at the inlet of the computational domain that is 25mm from the vertical block (when g/w = 8.0 and l/b = 1.5); and, the u_i is the velocity recorded at middle of the bounded region by the two parallel horizontal blocks that is 100mm from the inlet to the parallel blocks (refer to Figure 7). One can observe from Figure 12 that the increase of g/w ratio causes an increase in u_i/u_o. This phenomenon is proven in all l/b ratio tests. The bigger gap g allows more flowing water capacity into the location of u_i, and hence increase u_i velocity. Also observable, u_i/u_o profile becomes higher when l/b ratio increases (refer to Figure 12). Due to the use of smaller obstacle at the flow entrance i.e. smaller l, stronger vortices are created at the back of the $l \times b$ vertical block; and these vortices deviate the flow to give smaller u_i.

In terms for the comparison of the numerical predictions and the experimental measurements, it could be clearly observed that the k-ε numerical simulations predict the experimental measurements with a close correspondence at g/w > 4.0 for all l/b ratio tests; however, this consistency has vanished at 2.0 ≤ g/w ≤ 4.0. These results comparison shows that the k-ε model simulates the multi-obstruction flow well with big gap g in between the vertical block and the parallel horizontal blocks; but inconsistent to reproduce the actual flow field for the tests with small gap g. In the formulation of the k-ε model, the secondary current caused by the Reynolds decomposed lateral and vertical velocity fluctuations, v` and $w$`, is overlooked. Hence, in the tests with small gap g, where the strong turbulent field exists (associate with strong secondary current induction), the k-ε model shows incompetence predictions. However, for the obstructed-flows with relatively big gap g, the usage of the k-ε model is encouraged, since it is proven to reproduce close predictions to the experimental measurements without the expensive numerical representation of secondary current.

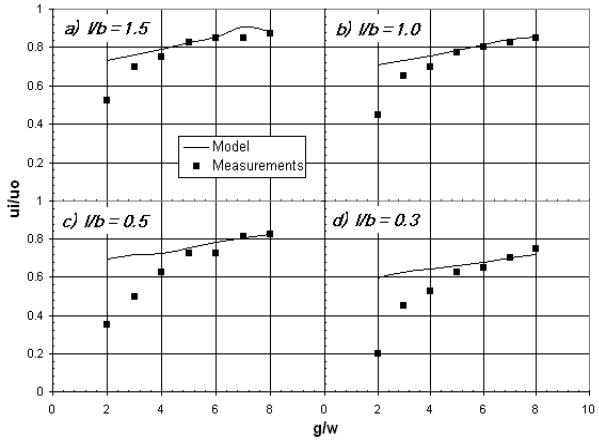

Fig. 12. u_i/u_o comparison of a) l/b = 1.5, b) l/b= 1.0, c) l/b= 0.5, and d) l/b= 0.3.

Conclusively, this study has established a clear proof to the limit of the k-ε model to represent the tested multiple obstruction flow, which one could summaries that the k-ε model is only sufficient to represent the presented multiple obstruction flow when g/w > 4.0. To further demonstrate the points mentioned above, the error analysis is done using

the L_2 norm at equation (35). In Table 1, it could be observed that the average relative error is sufficiently improved from the numerical predictions at $2.0 \leq g/w \leq 4.0$ to $4.0 < g/w \leq 8.0$. Furthermore, this efficiency of numerical predictions at $4.0 < g/w \leq 8.0$ is consistent for the *l/b* ratios tested, which shows that the *k-ε* model is consistent regardless the size of the vertical block.

Conclusions

As illustrated by researches in various literatures, the popular *k-ε* model has limitation in representing the turbulent flow applications. Inspired by this problem, in this paper, a quantitative assessment was developed to analyse the applicability of the *k-ε* model in predicting obstructions-induced discontinuous flows.

In this study, a combination of *k-ε* shallow water finite volume model with HLL approximate Riemann solver was presented. The MUSCL Hancock two-stage predictor-corrector scheme was used for the discretization of the model. The presented model was used to investigate the shallow water channel flow with the existence of obstructions. With suitable modifications, the proposed model could improve related processes of chemical fluids simulation and optimization. Two tests have been conducted to assess the ability of the presented model, single-obstruction and multi-obstruction flows. The presented model has reproduced relatively consistent results when compared against DNS simulations and experimental measurements from literatures.

In the first single obstruction induced discontinuous flow test, the *k-ε* shallow water model is proven to simulate the DNS results from literature closely. The *k-ε* function gives a significant improvement to the shallow water model by introducing the flow viscosity variation and the energy loss into the flow system. The second test further demonstrates that the *k-ε* shallow water model has conditionally well-predicted the discontinuous flow that induced by multiple obstructions. In this test, the *k-ε* shallow water model simulates close correspondence with the experimental measurements from literature when relatively big gap existed between the obstructions; however, it does not work well when the gap size is small. The modelling computational limit of gap ratio $g/w = 4.0$ between the obstructions is identified for this test, where it marks the limit for the *k-ε* shallow water model to simulate the multiple obstruction induced discontinuous flow. This limit further establishes a useful guideline for future *k-ε* turbulent numerical modelling researches on this type of multiple obstruction induced flow.

Acknowledgement

The first author would like to thank Dr Khalid Hussain and Prof Simon Tait at the University of Bradford, UK for their guidance on the SWE modelling during his PhD study. The authors also would like to acknowledge the research support from Prof Stefaan Simons and Prof Sergey Mikhalovsky at Nazarbayev University, Kazakhstan during the preparation of the manuscript. The first author also acknowledges support to this research from the Nazarbayev University Research Council Seed Grant, entitled 'Environmental Assessment of Sediment Pollution Impact on Hydropower Plants'.

References

1. Bosch, G. & Rodi, W. (1998). Simulation of vortex shedding past a square cylinder with different turbulent models. *International Journal of Numerical Method in Fluids*, 28, 601-616.
2. Harten, A., Lax, P. D. & van Leer, B. (1983). On upstream differencing and godunov-type schemes for hyperbolic conservation laws. *SIAM Review*, 25, No. 1, 35-61.
3. Horritt, M. (2004). Development and testing of a simple 2D finite volume model of sub-critical shallow water flow. *International Journal of Numerical Methods in Fluids*, 44,1231-1255.
4. Jiang, C. B., Yang, C. & Liang, D. F. (2009). Computation of shallow wakes with the fractional step finite element method. *Journal of Hydraulic Research*, 47, No. 1, 127-136.
5. Kabir, M. A., Khan, M. M. K. & Bhuiyan, M. A. (2004). Flow phenomena in a channel with different shaped obstructions at the entrance. *Fluid Dynamics Research*, 35, 391-408.
6. Lai, J. S., Lin, G. F. & Guo, W. D. (2005). An upstream flux-splitting finite-volume scheme for 2D shallow water equations. *International Journal of Numerical Methods in Fluids*, 48, 1149-1174.
7. Launder, B. E. & Spalding, D. B. (1974). The numerical computation of turbulent flows.

Computer Methods in Applied Mechanics and Engineering, 3, No. 2, 269-289.
8. Lee, T. S. (1998). Early stages of an impulsively started unsteady laminar flow past tapered trapezoidal cylinders. *International Journal of Numerical Method in Fluids*, 26, 1181-1203.
9. Mingham, C. G. & Causon, D. M. (2000). Calculation of unsteady bore diffraction using a high resolution finite volume method. *Journal of Hydraulic Research*, 38, No. 1, 49-56.
10. Osher, S. & Solomone, F. (1982). Upwind difference schemes for hyperbolic systems of conservation laws. *Mathematics and Computers in Simulation*, 38, 339 –374.
11. Pu, J. H. Efficient finite volume numerical modelling and experimental study of 2D shallow water free surface turbulent flows. *PhD Dissertation*, University of Bradford, Bradford, UK, 2008.
12. Pu, J. H., Hussain, K. & Tait, S. J. (2007). Simulation of turbulent free surface obstructed flow within channels. *Proceedings in the 32nd Congress of IAHR – Harmonizing the Demands of Art and Nature in Hydraulics*, Venice, Italy, *Theme A1*, pp. 1-8.
13. Rodi, W. Turbulence models and their application in hydraulics - a state of the art review. *International Association for Hydraulic Research, Netherlands*, 1980.
14. Roe, P. L. (1981). Approximate Riemann solvers, parameter vectors, and difference schemes. *Journal of Computational Physics*, 43, 357–372.
15. Sana, A., Ghumman, A. R. & Tanaka, H. (2009). Modeling of a rough-wall oscillatory boundary layer using two-equation turbulence models. *Journal of Hydraulic Engineering*, 135, No. 1, 60-65.
16. Sanders, B. F. (2001). High-resolution and non-oscillatory solution of the St. Venant equations in non-rectangular and non-prismatic channels. *Journal of Hydraulic Research*, 39, No. 3, 321-330.
17. Stansby, P. K. (1997). Semi-implicit finite volume shallow-water flow and solute transport solver with k-ε turbulent model. *International Journal of Numerical Methods in Fluids*, 25, 285-313.
18. Toro, E. F. Riemann solvers and numerical methods for fluid dynamics – a practical introduction. 2nd Edition, *Spring-Verlag Berlin Heidelberg*, 1999.
19. Tseng, M. H. (1999). Explicit finite volume non-oscillatory schemes for 2D transient free-surface flows. *International Journal of Numerical Method in Fluids*, 30, 831-843.
20. Wissink, J. G. (1997). DNS of 2D turbulent flow around a square cylinder. *International Journal for Numerical Methods in Fluids*, 25, 51-62.
21. Younus, M. and Chaudhry, M. H. (1994). A depth-averaged k-ε turbulent model for the computation of free-surface flow. *Journal of Hydraulic Research*, 32, No. 3, 415-444.

Received 3 November 2011